

Full Length Article

Mechanisms of tripartite permeability evolution for supercritical CO₂ in propped shale fractures

Lei Hou^{a,*}, Derek Elsworth^b^a School of Engineering, The University of Warwick, Coventry CV4 7AL, UK^b Energy and Mineral Engineering & Geosciences, EMS Energy Institute and G3 Center, Pennsylvania State University, University Park 16802, USA

ARTICLE INFO

Keywords:

Propped shale fracture
Adsorption
Permeability
Clay
Supercritical CO₂

ABSTRACT

Characterization of CO₂ flow in propped fractures is important in defining the response to CO₂ injection for reservoir stimulation and CO₂ sequestration. We measure the evolution of permeability in propped fractures of shale to both adsorbing CO₂ and non-adsorbing He under sub- and super-critical conditions. A tripartite permeability-pressure evolution curve is obtained when supercritical, consisting of a dual-U-shaped evolution first below and then exceeding critical pressure with a V-shaped fluctuation spanning the phase transition. The increasing adsorbed-phase-density and resultant swelling stress may control the permeability variation around the critical point. The inorganic adsorbent (mainly clay) may contribute to the secondary U-shaped evolution according to its sorption isotherm. The secondary adsorption may be generated by increasing sorption sites (competitive adsorption between CO₂ and H₂O) or through multi-layered sorption and stronger diffusion of supercritical CO₂. Further constraint is applied through observations of permeability recovery between initial and repeat saturations to non-adsorptive He. An abnormal increment of permeability recovery ratio is obtained for secondary adsorption, which may be caused by the dehydration and shrinkage of the matrix and the dissolution of minerals. Mechanisms of permeability evolution for CO₂ in shale are classified between organic and inorganic fractions. The contributions of adsorption to the permeability evolution are quantified by comparisons for permeation by CH₄ and He. A flat X-shaped trend is apparent, in which the inorganic contribution to permeability increases with increasing pressure while the organic contribution to permeability decreases with increasing pressure. The ratio of inorganic contribution reaches 60–70% under supercritical conditions.

1. Introduction

CO₂ injection in reservoirs (oil, gas or coal) is a promising approach for both enhancing the recovery of native hydrocarbons and for sequestering carbon emissions. These techniques include CO₂ flooding [10], fracturing [20], replacement [26] and storage in saline aquifers or depleted reservoirs [5,9]. A typical flow path of CO₂ in a reservoir is shown in Fig. 1, where CO₂ flows in through a well (1), then propped fractures (2) and finally into the porous medium (3). This injection may exert significant impacts on the stimulated reservoir volume (SRV) for hydrocarbon (oil and gas) recovery and sealing behaviour for carbon (CO₂) sequestration [33,41].

Abundant work has examined CO₂ flows in porous media to define interactions between gas and matrix and the corresponding effect on both permeabilities [2,51,52] and the mechanical properties of rock [47,48]. Less clarity is available for CO₂ flow in propped fractures,

where additional complexity is added with grain-fracture interactions to CO₂. Previous work has focussed on grain-fracture interactions to evaluate permeability loss by embedment under various conditions of closure stress, mineral composition, reservoir temperature and fracturing fluids [3,23,40]. Impacts of CO₂-matrix interaction (such as swelling) are relatively less prominent, especially for shales because of their lower organic contents. However, recent studies in high-organic-content Green River shale indicates that swelling could consume as much as 50% of the permeability and increase embedment by a factor of ~ 2 [19].

The measurement of permeability is one principal methodology characterizing the evolution of CO₂ fracture flow, which reflects the effects of both swelling and embedment [43,44]. A sorbing permeant (CO₂, CH₄ or N₂) swells the rock matrix and forms a typical U-shaped curve for permeability evolution with pressure due to the competition between adsorption and effective stress [25,28]. Nonetheless, the

* Corresponding author.

E-mail address: lei.hou@warwick.ac.uk (L. Hou).

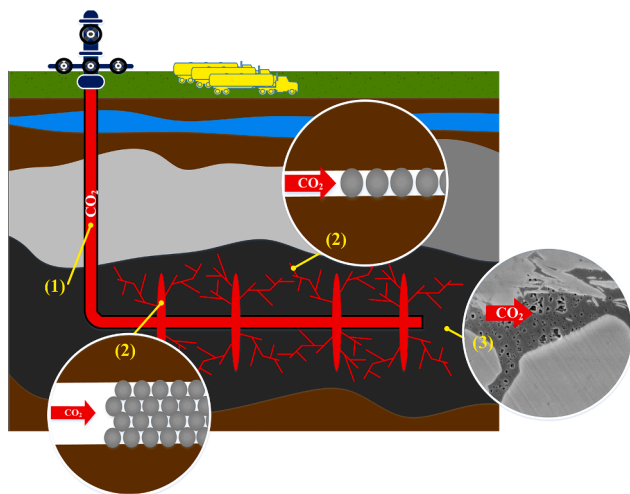


Fig. 1. Schematic of CO₂ injection in a shale reservoir through (1) a well, (2) propped fractures (main and branching fractures) and (3) the porous medium.

underlying mechanisms of adsorption-permeability response for CO₂ permeation in propped fractures remain unclear, due to a variety of factors, including:

- (1) Clues to the behaviour may be found in the response to CO₂ adsorption, although the common use of powdered rocks rather than the intact samples [24] limits the applicability of observations to fracture flow. The cubic dependence of permeability on fracture aperture magnifies the effect of swelling, thus leading to the appearance that the swelling of a trace content of organics may significantly impact permeability. A similar response is reported in the study of CO₂-clay interactions, where the stiffness of an intact sample may develop higher swelling stress than pure clay could under the same conditions [49].
- (2) Swelling of clay minerals is another controlling mechanism. An increasing number of studies reveal a strong positive correlation of shale clay content to sorption capacity of CO₂ [11,16,30,42]. CO₂ sorption capacity of powdered montmorillonite is comparable to that of coal [36]. However, excess exposure to supercritical CO₂ may conversely lead to shrinkage of clay by interlayer dehydration [1,29,34]. More experiments are needed to constrain the effect of such swelling-shrinking response on permeability evolution.
- (3) The CO₂ phase transition is observed to dramatically change permeability in simple powders [21], intact coal [50] and propped fractures in shale [19,28]. A sudden increase in density and kinetic energy may enhance the sorption capacity and plasticize the solid material to generate a precipitous drop in permeability around the critical point. However, more studies are required to constrain this permeability evolution under higher injection pressures where the CO₂ is in a supercritical state and for longer exposure.

Towards resolving these impacts, we explore CO₂-shale interactions across the sub- to super-critical phase transition in artificial (proxy-fluid-driven) fractures. We measure permeability evolution with the injection of both non-adsorptive helium (He) and adsorptive carbon dioxide (CO₂) on samples of Green River shale to (i) fully reveal the interaction process from sub- to super-critical pressure, (ii) define the different controlling mechanisms for permeability evolution in different stages of gas injection, and (iii) quantitatively analyze the contributions of each mechanism to provide a mechanistic understanding of characteristics of CO₂ fracture-flow towards improving the practice of oil/gas production and CO₂ sequestration.

2. Methodology

We measure permeability evolution to CO₂ and He in propped fractures in shale via pressure transient (pulse) methods. The apparatus (core holder and reservoirs) is immersed within a temperature-controlled water bath to control the state of CO₂, as either sub- or super-critical. We measure permeability to CO₂ and He alternately in the same sample to reveal the influence of adsorption and desorption behaviour.

2.1. Materials and preparation

Axially-split core samples (25 mm diameter 50 mm length) of Green River shale are packed with tape then placed in a pressurized core holder with monolayer proppant (40/80 mesh, Carbo-Lite ceramic proppant) sandwiched within the fracture. We explore the behaviour of a monolayer since the branch fractures or micro-fractures (usually monolayer-propped) compose a crucial component of the total stimulated reservoir volume [14,18,45]. Besides, similar permeating behaviour of CO₂ has been observed for both multi- and mono-layer propped samples, in which the monolayered sample exhibits an amplified swelling effect [28]. We use sorbing CO₂ (purity of 99.995%) and effectively-nonsorbing He (99.999%) as contrasting permeants for the permeability measurements.

2.2. Apparatus

A standard triaxial apparatus, as shown in Fig. 2, is used as the pressurized core holder (Temco). Both confining and axial stresses to 25 MPa are applied by syringe pumps (ISCO 500D) to a resolution of ± 0.007 MPa. A Viton rubber jacket is applied to seal and isolate the sample from the confining fluid in the core holder. Reservoir volumes are 26.7 ml for the upstream and 16.8 ml for the downstream with reservoir pressures measured by transducers (Omega PX302-2KGV and Omega PX302-5KGV) to resolutions of ± 0.03 MPa. Each transducer is calibrated for each new sample with National Instruments Labview used for data acquisition and pump control. The tests are performed at both room temperature (23 °C) and supercritical temperature (45 °C for a supercritical transition at 31 °C) in a water bath with the core holder and reservoirs immersed, as shown in Fig. 2. Interior gas pressures in the range 2 to 13 MPa access the various phase states of CO₂.

2.3. Procedure

We use standard pressure transient (pulse) methods for permeability measurements. A pressure difference (pulse) is applied between upstream and downstream and its upstream decay and downstream build-up behaviour is recorded and analysed to obtain the permeability that is calculated as [7],

$$k = \frac{\alpha\mu\beta LV_{up}V_{dn}}{A(V_{up} + V_{dn})} \quad (1)$$

where α is the slope of pressure decay against the logarithm of time; μ and β are the viscosity and compressibility of the fluid, respectively; L is the length of the sample; V_{up} and V_{dn} are volumes of the upstream and downstream reservoirs, respectively; and A is the fluid flow cross-sectional area in fracture (permeation through the rock matrix is ignored).

The compressibility of the fluid β is calculated from the bulk modulus

$$\beta = \frac{1}{B_M} = \frac{1}{v^2\rho} \quad (2)$$

where B_M is the bulk modulus of the fluid; v is the speed of sound in the fluid; ρ is the fluid density. The values of v and ρ are recovered from standard characterizations (National Institute of Standards and

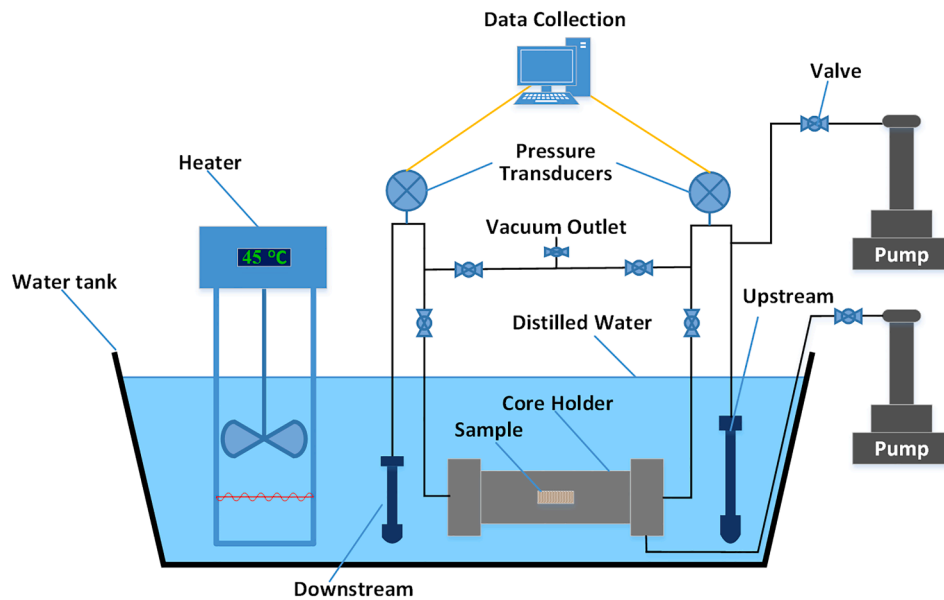


Fig. 2. Schematic of the experimental apparatus and water bath system [19,43].

Technology (NIST)). The values of compressibility are calculated and plotted in Fig. 3.

3. Results

Four groups of permeability measurements are conducted and summarized in Table 1. Five rounds of experiments are carried out in Group 1 for He and CO₂ as gaseous, liquid then supercritical state. The first four rounds are completed at room temperature (23 °C) with the final performed at a temperature of 45 °C beginning at a supercritical pressure. In particular, the permeability to non-sorbing He is repetitively measured in the same sample before and after the permeation of CO₂ to compare the impact of CO₂ adsorption and desorption. Each round of experiments involved in Group 2 is conducted continuously at 45 °C. Control Group 3 and 4 repeat sub- and super-critical pressure measurements with non-sorbing He.

Observations recovered by probing with both injection (increasing gas pressure) then depletion (decreasing gas pressure) are plotted in Fig. 4. Generally, positive parallel linear relationships are recovered between increasing gas pressure and increasing permeability for all cases of He and liquid CO₂, indicating that deformations under changes in effective stress (confining pressure minus injection pressure)

Table 1

Matrix of experiments defining samples and conditions.

Sample Type	Green River Shale			
Group No.	Experimental Group 1	Experimental Group 2	Control Group 3	Control Group 4
Injection Pressure	3 ~ 13 MPa	2 ~ 12 MPa	2 ~ 13 MPa	2 ~ 9 MPa
Temperature	23 °C & 45 °C	45 °C	23 °C	23 °C
CO ₂ Phases	Gaseous, Liquid & Supercritical	Supercritical	Gaseous	Gaseous
Dimensions	25 (dia.) * 50 (length) mm			
Proppant	Carbo-Lite Ceramite (40/80 Mesh)			
Gas	Helium & Carbon Dioxide			
Triaxial Pressure	25 MPa			

dominate the permeability evolution. This is expected for non-adsorptive He since swelling is absent. For liquid CO₂, with permeability one order-of-magnitude lower than that for He, a swelling effect may be manifest but is counteracted by the high injection pressure.

For the remainder of the CO₂ cases, typical U-shaped curves are observed under subcritical pressures as the result of the competition between adsorption and effective stress. A new U-shaped curve under

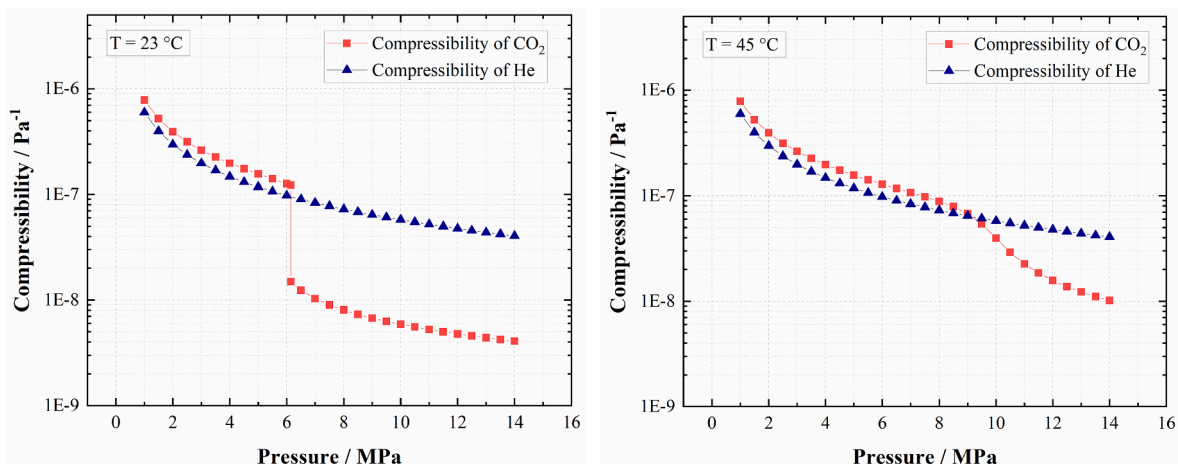


Fig. 3. Compressibility of CO₂ and He (based on NIST database).

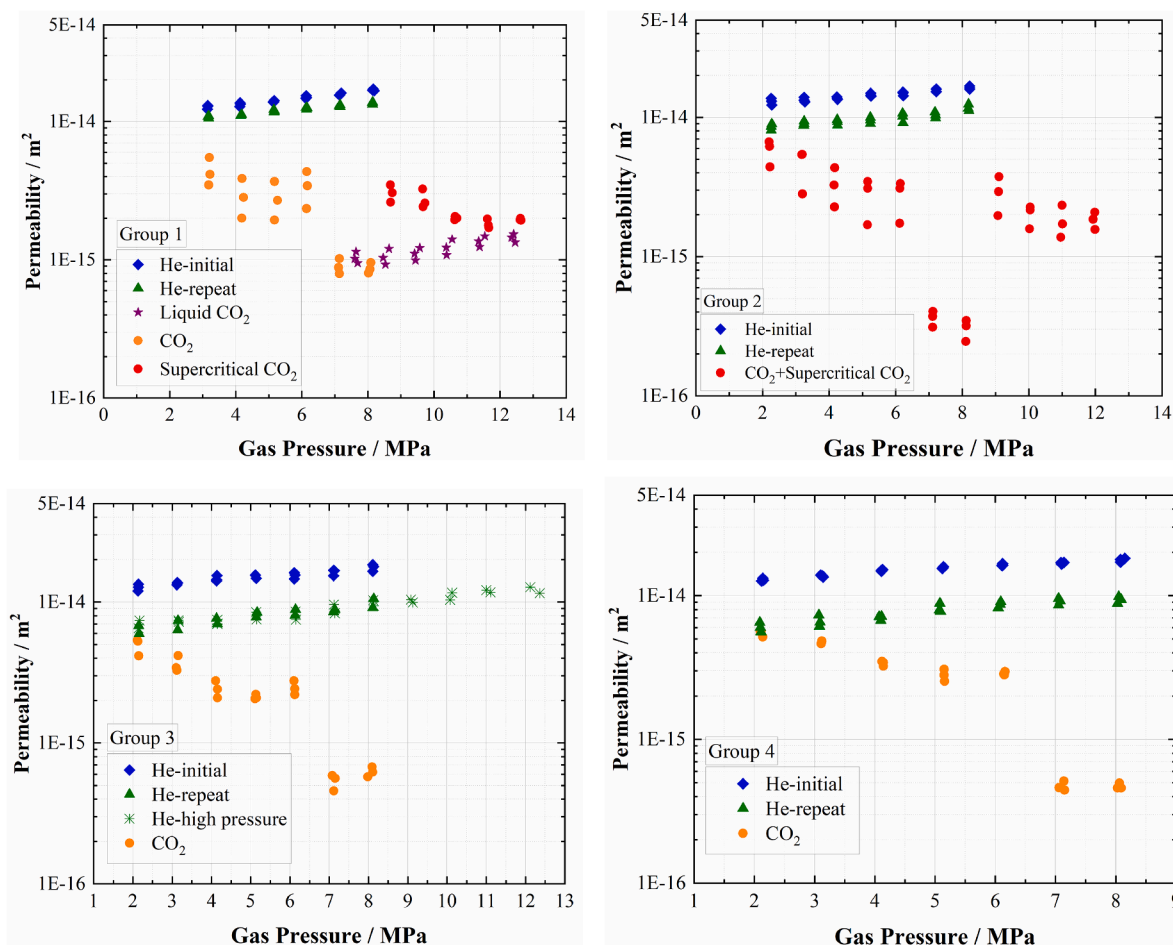


Fig. 4. Permeability evolution versus gas pressure in propped fractures in Green River shale. The repeat He tests are performed after all CO₂ tests in the same sample of each group. Group 2 is completed at 45 °C. Group 3 and 4 are at 23 °C. Group 1 is conducted at both temperatures and for various CO₂ phases. (For interpretation of the references to colour in this figure legend, the reader is referred to the web version of this article.)

high pressure is formed for the supercritical CO₂ cases. Results from all CO₂ cases are averaged and presented in Fig. 5. A tripartite permeating behaviour is apparent, consisting of (I) a typical U-shaped curve below the critical pressure, (II) a V-shaped fluctuation around the phase transition point and (III) a secondary U-shaped curve above supercritical

pressure and temperature. Part III exhibits a similar parabolic trend as Part I, and reaches the minimum value around a pressure of 11–12 MPa.

4. Discussion

The mechanism of permeability evolution in a propped fracture is described schematically in Fig. 6. Different from an intact simple with pores or natural micro-fractures at the nanometer-scale, the existence of proppant particles (1) provides a macroporous flow channel that is

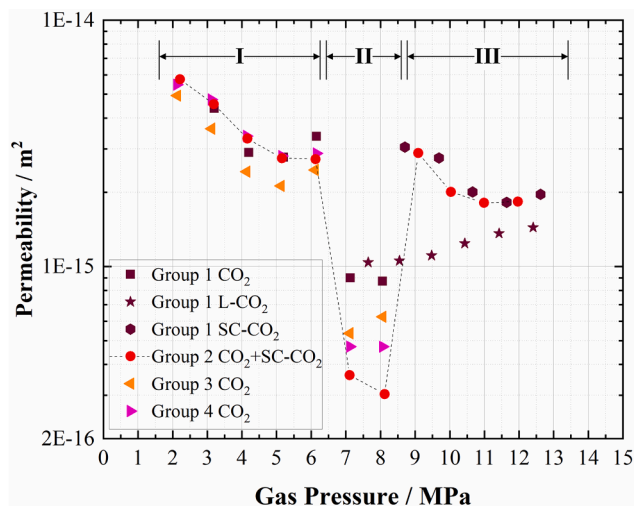


Fig. 5. Permeability evolution versus gas pressure for all CO₂ cases presented as averaged values.

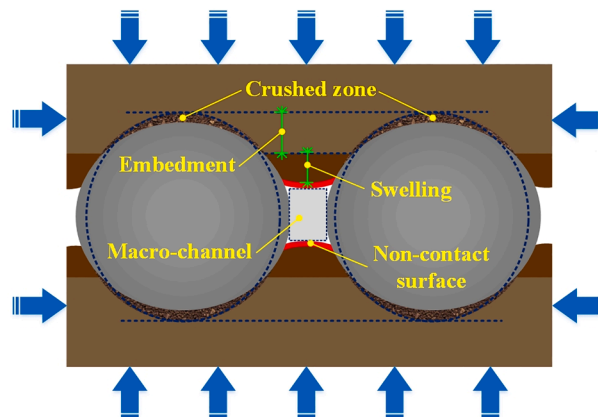


Fig. 6. Schematic of flow mechanisms of a propped fracture in shale.

modified by the synthetic impacts of effective stress, grain embedment and matrix swelling. The gap between grains (2) generates a pair of non-contacting surfaces, through which swelling magnifies the resulting fracture closure. The surface deformation of the fracture and the crushed zone between matrix and grains (3) increases the contact area with permeants and enhances the sorbing capacity. In addition, the mineral matter tends to be enriched in the crushed zone, which enhances permeant diffusion and sorption kinetics [39].

4.1. Influence of CO₂ phase transition

Permeability decreases precipitously at the beginning of phase transitions from gaseous to both liquid and supercritical states (Fig. 5). However, the influencing mechanisms may be different between these liquid and supercritical transitions – suggested by the differences in the subsequent permeability trends at high pressure. The permeation of liquid CO₂ remains continuous for the overlapping pressure from 7 to 9 MPa (Group 1 L-CO₂ in Fig. 5). In contrast, the permeability to supercritical CO₂ (SC-CO₂) emerges as a direct climb back to the subcritical level. The liquid case is explained by the sudden volume change during the phase transition for a relatively stable pressure [28]. For the supercritical case, the effective aperture variation may be controlled by adsorbed mass and effective stress, graphically described in Fig. 7.

The phase change of CO₂ near the critical point results in a sharp increase in adsorbed phase density and its resultant swelling strain [4], which compresses the effective aperture and induces a drop in permeability, as shown in Fig. 7(a). The severe swelling strain may consume ~80% of the effective aperture [19]. Swelling stresses of 9.6–24.7 MPa may result upon introduction of CO₂ at 10 MPa and 44 °C measured by uniaxial compaction/swelling test on montmorillonite and shale [49]. The swelling stress converts into a free-swelling strain enabled by the non-contacting surfaces (Fig. 6). With increasing swelling, the cumulative stress opposes and overcomes the confining pressure then partly releases the confining-stress-compressed aperture (Fig. 7(b)) – increasing permeability at the conclusion of the phase transition. The presence of an artificial fracture and grains liberates the swelling stress opposing the confining pressure, which is the essential difference with the intact sample that retains the swelling stress within the rock structure [50].

4.2. Dual-U-shaped evolution due to secondary adsorption in clay

Similar concave-upwards evolutions of permeability are present in Parts I and III of the response which may result from secondary adsorption of CO₂. Direct evidence is reported in studies of CO₂-clay interactions. The isotherms show dual-inverted-parabolic fluctuations at pressures above ~8–12 MPa in Muderong shale at the same temperature of 45 °C. This is attributed to CO₂ adsorption in clay because of the

consistent pattern with the isotherm of pure clay (Kaolinite), as shown in Fig. 8(a) [8]. At micropore scale, the CO₂ pore density (sum of the bulk fluid density and pore volume normalized excess density) in the clay (montmorillonite) pore is estimated by combining the data for excess sorption and interlayer thickness measurements. A similar evolution curve is observed in Fig. 8(b), which is induced by the entrance of supercritical CO₂ into the inter-molecular layer space within the clay and multilayer sorption at higher fluid density [37]. More evidence is apparent in experiments on Texas and Wyoming clays [36] and Utica shale [38].

CO₂ adsorption induces swelling strain that consumes the effective aperture in the propped fracture, thus decreasing permeability with increased swelling. The M-shaped isotherms of CO₂ in clay (Fig. 8) are the inverse (reflection) of the dual-U-shaped permeability curves (Fig. 5). The pressures corresponding to the second peak values of adsorption and CO₂ pore density are 11.7 MPa and 12.2 MPa, respectively, which agree with the pressure (11–12 MPa) corresponding to the trough in the second valley in permeability magnitude in Part III. The previous study of real-time X-ray CT analysis indicates that clay- and inertite-rich micro-lithotypes hold most of the CO₂ adsorption increment with increasing gas pressure because of their high porosity [22]. It may infer that the CO₂ adsorption in clay dominates the secondary permeability evolution.

4.3. Generation of secondary adsorption and impact on permeability recovery

The difference in response both with (Group 1 and 2) and without (Group 3 and 4) the secondary adsorption (Part III) is reflected in the permeability recovery between initial and repeat He cases, as shown in Fig. 9. The permeation of CO₂ swells and softens the rock matrix, which intensifies the irreversible embedment of grains then restrains the permeability recovery ratio [19]. Only ~52% of the permeability, on average, recovers in Groups 3 and 4. For Groups 1 and 2, the secondary adsorption of supercritical CO₂ could prompt increased embedment that should have reduced the permeability recovery. In contrast, it raises the permeability to ~79% and ~68% in Groups 1 and 2, respectively.

The mechanism of secondary adsorption may result in such abnormal phenomena. The phase transition of CO₂ into a supercritical state increases the binding energy, which may break the balance of competitive adsorption between CO₂ and H₂O then dehydrate the clay or other water-containing constituents [6]. The macropore flow-channel (Fig. 6) aids this effusion of fugitive water. The sorption site occupied by a water molecule vacates enough space for 2.2 CO₂ molecules [17]. Besides, the increasing density of supercritical CO₂ generates more molecular layers attaching to the surface, thus enhancing the total absorbed mass [24,37]. The higher diffusibility of supercritical CO₂ also increases the interaction surfaces by diffusing into more pores and

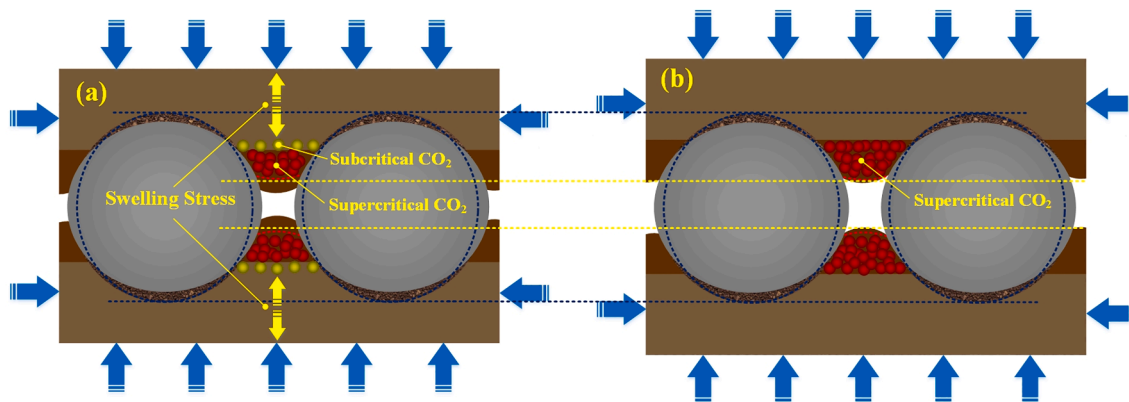


Fig. 7. Schematics of effective aperture evolution (a) during the phase transition and (b) under supercritical state.

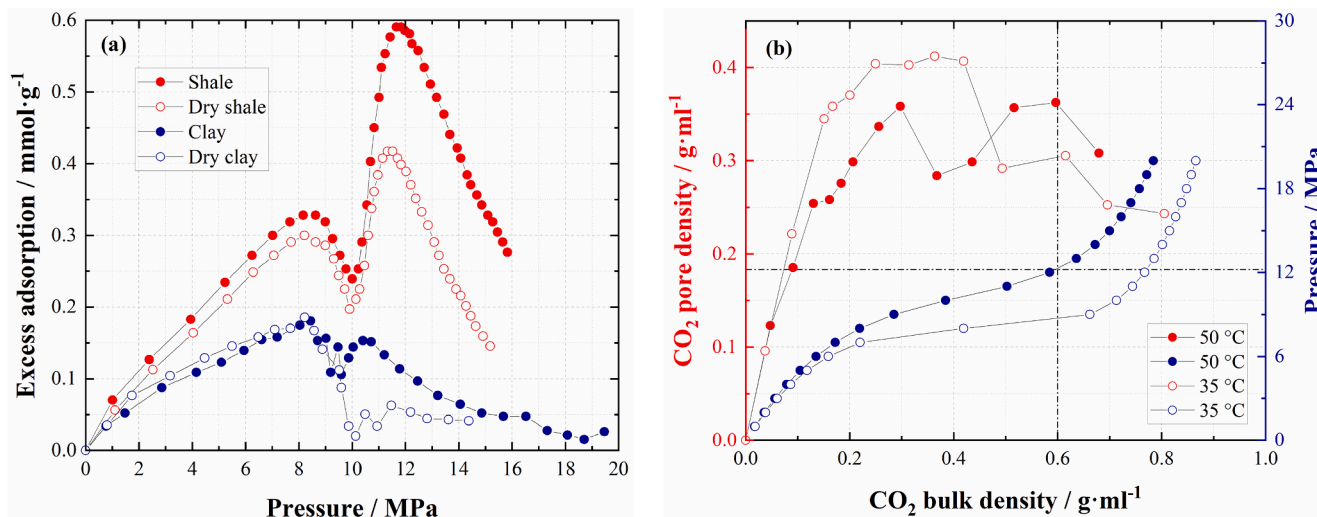


Fig. 8. CO₂ adsorption in shale and clay. (a) Excess adsorption in Muderong shale and kaolinite at 45 °C [8]; (b) CO₂ pore density in montmorillonite as a function of bulk density and corresponding pressure [37].

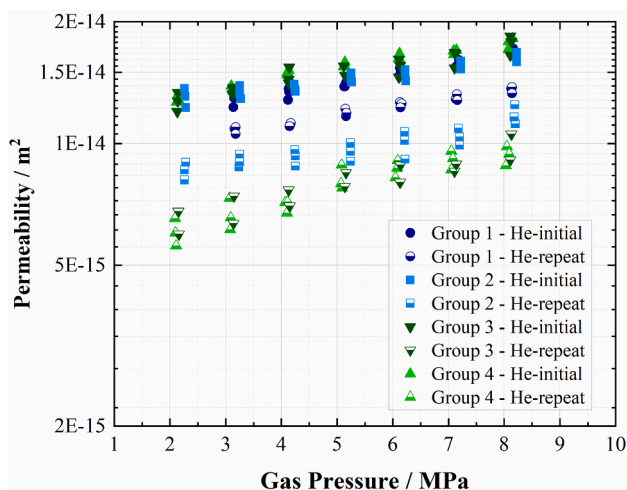


Fig. 9. Permeability recovery of non-sorbing He both before (initial) and then after (repeat) the injection of sorbing CO₂.

deeper into the matrix [27,31]. Therefore, increasing sorption sites, enabling sorption of multi-layered molecules and increased diffusion rate of supercritical CO₂ may all contribute to secondary-adsorption (Fig. 5).

Subsequently, the dehydration induces shrinkage of the rock matrix and increases the effective aperture that follows a cubic law with permeability [12,35]. Moreover, the dissolution of minerals resulting from the co-existence of CO₂ in water may additionally enlarge the effective aperture [46], particularly for the Green River shale with a high content of carbonates (Dolomite 39.4% and Calcite 12.4%) [13]. This may further explain the different recovery ratios between Group 1 and 2 experiments, where the longer CO₂ exposure leads to greater carbonate dissolution and higher permeability recovery for Group 1. The irreversible shrinkage and dissolution enlargement after the desorption of CO₂ in the repeat-He case may contribute to the abnormal increment of permeability recovery.

4.4. Contributions of organic and inorganic adsorptions to permeability evolution

The contributions of organic and inorganic adsorptions to the dual-

U-shaped permeability evolution are estimated based on assumptions that (1) the permeability is a sum of functions of organic adsorption- $f(Org_{ads})$, inorganic adsorption- $f(Inorg_{ads})$ and effective stress- $f(Effective\ Stress)$, in which (2) the adsorption functions ($f(Org_{ads})$, $f(Inorg_{ads})$) are inversely proportional to adsorption masses. According to assumption (1), the permeability of the adsorptive permeant may be calculated from

$$Perm = f(Org_{ads}, Inorg_{ads}, Effective\ Stress) = af(Org_{ads}) + bf(Inorg_{ads}) + cf(Effective\ Stress) \quad (3)$$

where Org_{ads} and $Inorg_{ads}$ are the adsorption masses of the permeant in the organic and inorganic constituents, respectively. a , b and c are coefficients and all assigned the value of 1 in this study.

The permeability evolution of CH₄ in Green River shale is utilized for a comparative analysis since the adsorption occurs mainly in the organics, as shown in Fig. 10 [46]. As the TOC content reduces, the CH₄ adsorption in shale approaches zero and yet residual CO₂ adsorption remains in the inorganic constituents under the same condition. Similar results are reported in experiments on shales from the United States [15] and South China [53]. The maximum sorption capacity of CH₄ commonly appears at a lower pressure than that of CO₂, even in the same shale. Largely pressures to CO₂ and CH₄ in a group of split tests are

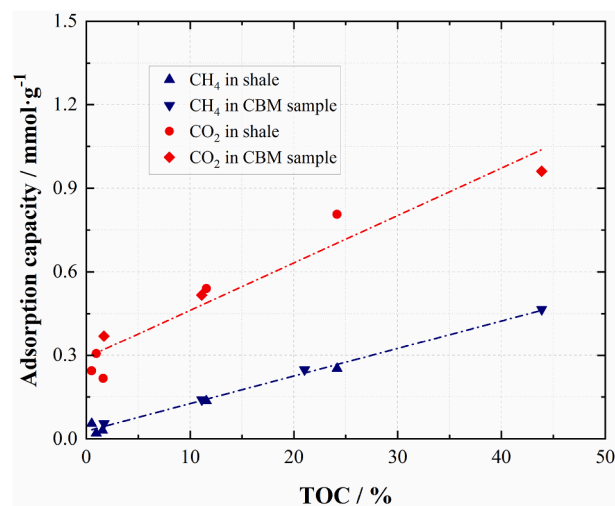


Fig. 10. Adsorption capacities of CH₄ and CO₂ versus TOC (in shale and CBM sample, 45 °C and ~ 12 MPa) [46].

approximately a factor of two different (Table 2). The corresponding pressures of the minimum permeability in Part III (11–12 MPa) and I (5–6 MPa) are also offset by a factor of two, as shown in Fig. 5.

Based on assumption (2), the contribution ratio of CO₂ and CH₄ adsorption to permeability in organics in the same sample is expressed as

$$\frac{f(Or_{gads})_{CO_2}}{f(Or_{gads})_{CH_4}} = \frac{f(Adsorption\ Mass_{CO_2})}{f(Adsorption\ Mass_{CH_4})} = \frac{Adsorption\ Mass_{CH_4}}{Adsorption\ Mass_{CO_2}} \quad (4)$$

The adsorption masses under various pressures are estimated by the Langmuir model, in which the maximum adsorption volume and Langmuir pressure are fitted using the measurements in anthracite for its high carbon content (>90%), as shown in Fig. 11 [32].

Eq. (4) is then resolved as

$$\frac{f(Or_{gads})_{CO_2}}{f(Or_{gads})_{CH_4}} = \frac{Adsorption\ Mass_{CH_4}}{Adsorption\ Mass_{CO_2}} = \frac{5}{14} \frac{2 + P}{0.77 + P} \quad (5)$$

where P is the injection pressure, MPa.

The ratio of permeabilities under the same effective pressure in the same sample is calculated as

$$\frac{Perm_{CO_2}}{Perm_{He}} = \frac{f(Or_{gads})_{CO_2} + f(Inorg_{gads})_{CO_2} + f'(Effective\ Stress)}{f'(Effective\ Stress)} \quad (6)$$

and

$$\frac{Perm_{CH_4}}{Perm_{He}} = \frac{f(Or_{gads})_{CH_4} + f'(Effective\ Stress)}{f'(Effective\ Stress)} \quad (7)$$

where the adsorption of CH₄ in inorganics is ignored comparing with that of CO₂ (Fig. 10).

The normalization of Eqs. (6) and (7) relative to effective stress is applied to eliminate this effect in their intercomparisons. Then,

$$\frac{f(Or_{gads})_{CH_4}}{f(Or_{gads})_{CO_2} + f(Inorg_{gads})_{CO_2}} = \frac{Perm_{CH_4}/Perm_{He} - 1}{Perm_{CO_2}/Perm_{He} - 1} \quad (8)$$

We define the relative contribution of organic and inorganic adsorption to permeability evolution for the case of CO₂ as “Contribution ratio”. Combing Eqs. (5) and (8), it is estimated as

$$\begin{aligned} Contribution\ ratio_{Or_{gads}} &= \frac{f(Or_{gads})_{CO_2}}{f(Or_{gads})_{CO_2} + f(Inorg_{gads})_{CO_2}} \\ &= \frac{5}{14} \frac{2 + P}{0.77 + P} \frac{Perm_{CH_4}/Perm_{He} - 1}{Perm_{CO_2}/Perm_{He} - 1} \end{aligned} \quad (9)$$

$$Contribution\ ratio_{Inorg_{gads}} = 1 - Contribution\ rate_{Or_{gads}} \quad (10)$$

The averaged data from Groups 1 and 2 (Fig. 4), excluding the liquid CO₂ and He-repeat cases, are employed to define the permeabilities to CO₂ and He. The permeability to CH₄ is recovered from measurements using the same material (Green River shale and 40/80 Carbo-Lite proppant) and similar apparatus and procedures, as shown in Fig. 12

Table 2

Comparison of Langmuir pressure (P_L) between CO₂ and CH₄ in shale samples from Paraná Basin, Brazil [46].

No.	Rock Type	n_L CH ₄ mmol/g	P_L CH ₄ MPa	n_L CO ₂ mmol/g	P_L CO ₂ MPa	P_{LCO_2} / P_{LCH_4}
07_114	Carbonate	0.07	4.09	0.69	8.43	2.06
07_117/ 118	Shale	0.28	2.31	0.8	6.19	2.68
07_181		0.18	5.79	0.9	12.01	2.07
08_100	Shale	0.04	16.09	0.78	20	1.24
08_101		0.08	7.09	0.69	19.03	2.68
08_168		0.37	8.39	2.02	15	1.79
08_170		0.25	14.16	1.25	13.43	0.95
08_154		0.04	5.65	0.65	19.9	3.52

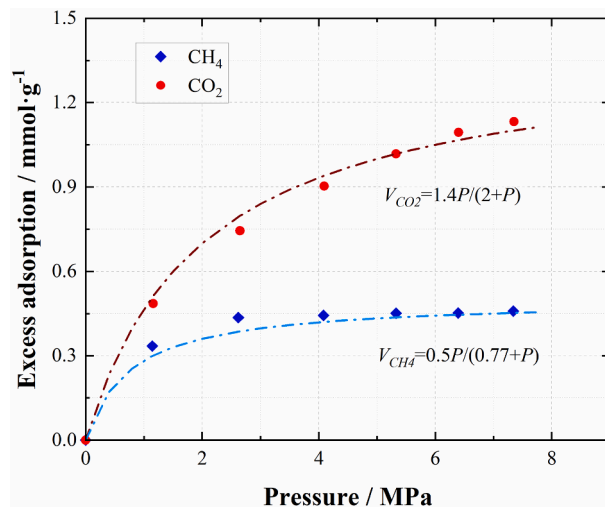


Fig. 11. Excess adsorption (45 °C) of CH₄ and CO₂ in anthracite and fitted Langmuir equations [32].

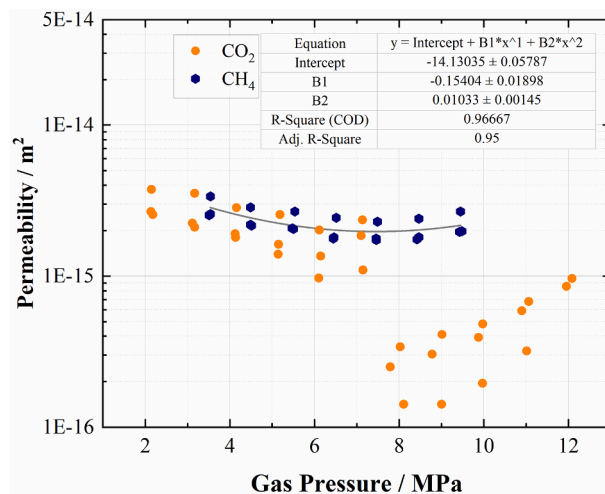


Fig. 12. Permeability evolution in Green River shale upon injection of CO₂ and CH₄ at a temperature of 21 °C and confining pressure of 20 MPa [28]. (For interpretation of the references to colour in this figure legend, the reader is referred to the web version of this article.)

[28]. The approximations for CO₂ permeability are reported and compared with those in Fig. 4.

The ratios of the contribution of organic and inorganic adsorption to permeability evolution are analyzed by Eqs. (9) and (10) and plotted in Fig. 13. A flat X-shaped curve is presented, in which the contribution of adsorption to the organic fraction decreases with increasing pressure, while the inorganic contribution increases with increasing pressure. Reflected in the tripartite permeability evolution, the effect of organic adsorption is initially dominant but decreases rapidly before flattening out in Part I. The effect of inorganic adsorption increases with increasing pressure before approaching the magnitude of the effect to that of organic adsorption under subcritical pressure. For the secondary adsorption of Part III, the inorganic constituents (mainly clay with high porosity and high surface area) provide most of the sorption sites and contribute 60–70% of the total adsorptive fractions that induce another U-shaped evolution of permeability under supercritical conditions. Similarly, the previous study of real-time X-ray CT scanning on the different positions of a coal sample shows that the vitrinite-liptinite-region and clay-inertinite-region adsorbed 19% and 81% of CO₂ (4.42 MPa), respectively [22].

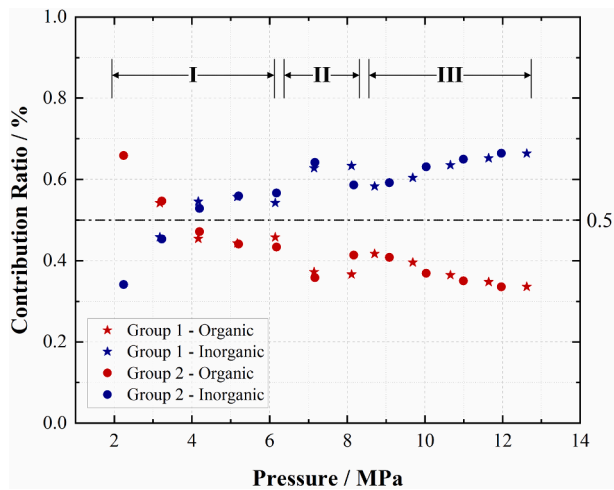


Fig. 13. Relative contribution ratio of organic and inorganic adsorptions to permeability evolution for supercritical CO₂ (45 °C) in the propped shale fracture.

5. Conclusions

Permeability evolution in propped shale fractures to non-adsorptive He and adsorptive CO₂ have been measured across both sub- and supercritical conditions. The CO₂-matrix and grain-to-surface interactions, CO₂ phase transition and their mutual effects are analysed to reveal mechanisms of permeability evolution. Contributions of CO₂ adsorption to permeability evolution are classified and quantified by comparing with responses to slightly-adsorptive CH₄ and non-adsorptive He. The main observations of this work are as follow:

- (1) A tripartite permeability curve is apparent for supercritical CO₂, including dual-U-shaped evolutions at pressures first below (I) and then exceeding (III) the critical point (pressure) with a precipitous V-shaped fluctuation during the intervening case of the phase transition (II). Different from the case of subcritical CO₂, the initial permeability drop at the beginning of the phase transition may be induced by an increase in the adsorbed-phase-density and the resulting swelling strain. The subsequent recovery of permeability may result from the accumulative swelling stress that overcomes the confining pressure and partly releases the confining-stress-compressed aperture.
- (2) The dual-U-shaped permeability evolution is controlled by CO₂ adsorptions. The phase transition of CO₂ may increase the binding energy that favors its competitive adsorption with H₂O and results in more sorption sites. Additionally, an increased diffusivity and density of supercritical CO₂ increases the interaction surface area and generates multilayer molecular sorption onto the surface, respectively. These synthetic factors result in a secondary-adsorption then a secondary-U-shaped permeability evolution at fluid pressures in excess of the critical condition.
- (3) The abnormal increments of permeability recovery for He-repeat cases in Groups 1 and 2 are observed where secondary-adsorption occurs. Dehydration by the competitive adsorption between CO₂ and H₂O shrinks the matrix, especially for the clay constituents. The accompanying process of mineral dissolution by the co-existence of CO₂ in water makes an extra contribution. Irreversible matrix shrinkage and mineral dissolution yield larger effective aperture that results in abnormal increments of permeability recovery after the desorption of CO₂.
- (4) Mechanisms of permeability evolution for CO₂ in shale are classified between organic and inorganic fractions. Each contribution to the permeability evolution is quantified by comparison

between CH₄ and He measurements. A flat X-shaped trend is apparent, in which the inorganic contribution increases rapidly with increasing pressure then flattens out while the organic contribution decreases rapidly with increasing pressure then levels off. The inorganic constituents (mainly clay with high porosity and large surface area) provide most of the sorption sites and contribute 60–70% of the total adsorptive fractions that result in the secondary-U-shaped permeability evolution under supercritical conditions.

CRedit authorship contribution statement

Lei Hou: Conceptualization, Methodology, Investigation, Writing - original draft. **Derek Elsworth:** Writing - review & editing, Resources, Supervision.

Declaration of Competing Interest

The authors declare that they have no known competing financial interests or personal relationships that could have appeared to influence the work reported in this paper.

Acknowledgements



This research has received funding from the European Union's Horizon 2020 research and innovation programme under the Marie Skłodowska-Curie grant agreement No 846775.

References

- [1] Akono A-T, Druhan JL, Dávila G, Tsotsis T, Jessen K, Fuchs S, Crandall D, Shi Z, Dalton L, Tkach MK, Goodman AL, Frailey S, Werth CJ. A review of geochemical-mechanical impacts in geological carbon storage reservoirs. *Greenhouse Gas Sci Technol* 2019;9(3):474–504.
- [2] Ao X, Lu Y, Tang J, Chen Y, Li H. Investigation on the physics structure and chemical properties of the shale treated by supercritical CO₂. *J CO₂ Util* 2017;20:274–81.
- [3] Arshadi M, Zolfaghari A, Piri M, Al-Muntasheri GA, Sayed M. The effect of deformation on two-phase flow through proppant-packed fractured shale samples: a micro-scale experimental investigation. *Adv Water Resour* 2017;105:108–31.
- [4] Bakhshian S, Hosseini SA. Prediction of CO₂ adsorption-induced deformation in shale nanopores. *Fuel* 2019;241:767–76.
- [5] Bielicki JM, Langenfeld JK, Tao Z, Middleton RS, Menefee AH, Clarens AF. The geospatial and economic viability of CO₂ storage in hydrocarbon depleted fractured shale formations. *Int J Greenhouse Gas Control* 2018;75:8–23.
- [6] Bowers GM, Schaefer HT, Loring JS, Hoyt DW, Burton SD, Walter ED, Kirkpatrick RJ. Role of cations in CO₂ adsorption, dynamics, and hydration in smectite clays under in situ supercritical CO₂ conditions. *J Phys Chem C* 2017;121(1):577–92.
- [7] Brace WF, Walsh JB, Frangos WT. Permeability of granite under high pressure. *J Geophys Res* 1968;73(6):2225–36.
- [8] Busch A, Alles S, Gensterblum Y, Prinz D, Dewhurst D, Raven M, Stanjek H, Krooss B. Carbon dioxide storage potential of shales. *Int J Greenhouse Gas Control* 2008;2(3):297–308.
- [9] Buscheck TA, White JA, Carrol SA, Bielicki JM, Aines RD. Managing geologic CO₂ storage with pre-injection brine production: a strategy evaluated with a model of CO₂ injection at Snøhvit. *Energy Environ Sci* 2016;9(4):1504–12.
- [10] Cao M, Gu Y. Oil recovery mechanisms and asphaltene precipitation phenomenon in immiscible and miscible CO₂ flooding processes. *Fuel* 2013;109:157–66.
- [11] Chalmers GRL, Bustin RM. Lower Cretaceous gas shales in northeastern British Columbia, Part I: geological controls on methane sorption capacity. *Bull Can Pet Geol* 2008;56(1):1–21.
- [12] Elsworth D, Goodman RE. Characterization of rock fissure hydraulic conductivity using idealized wall roughness profiles. *Int J Rock Mech Mining Sci Geomech Abstracts* 1986;23(3):233–43.
- [13] Fang Yi, Elsworth D, Wang C, Ishibashi T, Fitts JP. Frictional stability-permeability relationships for fractures in shales: friction-permeability relationships. *J Geophys Res Solid Earth* 2017;122(3):1760–76.

- [14] Gale JFW, Laubach SE, Olson JE, Eichhuble P, Fall A. Natural Fractures in shale: a review and new observations. *Bulletin* 2014;98(11):2165–2166.
- [15] Gasparik M, Bertier P, Gensterblum Y, Ghanizadeh A, Krooss BM, Littke R. Geological controls on the methane storage capacity in organic-rich shales. *Int J Coal Geol* 2014;123:34–51.
- [16] Gasparik M, Ghanizadeh A, Bertier P, Gensterblum Y, Bouw S, Krooss BM. High-pressure methane sorption isotherms of black Shales from The Netherlands. *Energy Fuels* 2012;26(8):4995–5004.
- [17] Gensterblum Y, Busch A, Krooss BM. Molecular concept and experimental evidence of competitive adsorption of H₂O, CO₂ and CH₄ on organic material. *Fuel* 2014;115:581–8.
- [18] Hoek E, Martin CD. Fracture initiation and propagation in intact rock – a review. *J Rock Mech Geotech Eng* 2014;6(4):287–300.
- [19] Hou L, Elsworth D, Geng X. Swelling and embedment induced by sub- and supercritical-CO₂ on the permeability of propped fractures in shale. *Int J Coal Geol* 2020;225:103496. <https://doi.org/10.1016/j.coal.2020.103496>.
- [20] Hou L, Jiang T, Liu He, Geng X, Sun B, Li G, Meng S. An evaluation method of supercritical CO₂ thickening result for particle transporting. *J CO₂ Util* 2017;21:247–52.
- [21] Jia B, Tsau J-S, Barati R. Different flow behaviors of low-pressure and high-pressure carbon dioxide in shales. *SPE J* 2018;23(04):1452–68. <https://doi.org/10.2118/191121-pa>.
- [22] Karacan CÖ, Mitchell GD. Behavior and effect of different coal microlithotypes during gas transport for carbon dioxide sequestration into coal seams. *Int J Coal Geol* 2003;53(4):201–17.
- [23] Kewen Li YG, Lyu Youchang. New mathematical models for calculating proppant embedment and fracture conductivity. *SPE J* 2015;20(03):1–12.
- [24] Klewiah I, Berawala DS, Alexander Walker HC, Andersen PØ, Nadeau PH. Review of experimental sorption studies of CO₂ and CH₄ in shales. *J Nat Gas Sci Eng* 2020;73:103045. <https://doi.org/10.1016/j.jngse.2019.103045>.
- [25] Kumar H, Elsworth D, Liu J, Pone D, Mathews JP. Permeability evolution of propped artificial fractures in coal on injection of CO₂. *J Petrol Sci Eng* 2015;133:695–704.
- [26] Lan Y, Yang Z, Wang P, Yan Y, Zhang Li, Ran J. A review of microscopic seepage mechanism for shale gas extracted by supercritical CO₂ flooding. *Fuel* 2019;238:412–24.
- [27] Li S, Li Z, Dong Q. Diffusion coefficients of supercritical CO₂ in oil-saturated cores under low permeability reservoir conditions. *J CO₂ Util* 2016;14:47–60.
- [28] Li X, Feng Z, Han G, Elsworth D, Marone C, Saffer D, Cheon D-S. Permeability evolution of propped artificial fractures in green river shale. *Rock Mech Rock Eng* 2017;50(6):1473–85.
- [29] Lu Y, Ao X, Tang J, Jia Y, Zhang X, Chen Y. Swelling of shale in supercritical carbon dioxide. *J Nat Gas Sci Eng* 2016;30:268–75.
- [30] Luo X, Wang S, Wang Z, Jing Z, Lv M, Zhai Z, Han T. Adsorption of methane, carbon dioxide and their binary mixtures on Jurassic shale from the Qaidam Basin in China. *Int J Coal Geol* 2015;150–151:210–23.
- [31] Lv J, Chi Y, Zhao C, Zhang Yi, Mu H. Experimental study of the supercritical CO₂ diffusion coefficient in porous media under reservoir conditions. *R Soc Open Sci* 2019;6(6):181902. <https://doi.org/10.1098/rsos.181902>.
- [32] Merkel A, Gensterblum Y, Krooss BM, Amann A. Competitive sorption of CH₄, CO₂ and H₂O on natural coals of different rank. *Int J Coal Geol* 2015;150–151:181–92.
- [33] Middleton RS, Carey JW, Currier RP, Hyman JD, Kang Q, Karra S, Jiménez-Martínez J, Porter ML, Viswanathan HS. Shale gas and non-aqueous fracturing fluids: opportunities and challenges for supercritical CO₂. *Appl Energy* 2015;147:500–9.
- [34] Pan Z, Connell LD. A theoretical model for gas adsorption-induced coal swelling. *Int J Coal Geol* 2007;69(4):243–52.
- [35] Piggott AR, Elsworth D. Laboratory assessment of the equivalent apertures of a rock fracture. *Geophys Res Lett* 1993;20(13):1387–90.
- [36] Romanov VN. Evidence of irreversible CO₂ intercalation in montmorillonite. *Int J Greenhouse Gas Control* 2013;14:220–6.
- [37] Rother G, Ilton ES, Wallacher D, Hauß T, Schaeff HT, Qafoku O, Rosso KM, Felmy AR, Krukowski EG, Stack AG, Grimm N, Bodnar RJ. CO₂ sorption to subsingle hydration layer montmorillonite clay studied by excess sorption and neutron diffraction measurements. *Environ Sci Technol* 2013;47(1):205–11.
- [38] Sanguinito S, Goodman A, Tkach M, Kutchko B, Culp J, Natesakhawat S, Fazio J, Fukai I, Crandall D. Quantifying dry supercritical CO₂-induced changes of the Utica Shale. *Fuel* 2018;226:54–64.
- [39] Spears DA, Booth CA. The composition of size-fractionated pulverised coal and the trace element associations. *Fuel* 2002;81(5):683–90.
- [40] Tang Y, Ranjith PG. An experimental and analytical study of the effects of shear displacement, fluid type, joint roughness, shear strength, friction angle and dilation angle on proppant embedment development in tight gas sandstone reservoirs. *Int J Rock Mech Min Sci* 2018;107:94–109.
- [41] Tayari F, Blumsack S. A real options approach to production and injection timing under uncertainty for CO₂ sequestration in depleted shale gas reservoirs. *Appl Energy* 2020;263:114491. <https://doi.org/10.1016/j.apenergy.2020.114491>.
- [42] Wang Lu, Yu Q. The effect of moisture on the methane adsorption capacity of shales: a study case in the eastern Qaidam Basin in China. *J Hydrol* 2016;542:487–505.
- [43] Wang S, Elsworth D, Liu J. Permeability evolution in fractured coal: the roles of fracture geometry and water-content. *Int J Coal Geol* 2011;87(1):13–25.
- [44] Wang S, Elsworth D, Liu J. Permeability evolution during progressive deformation of intact coal and implications for instability in underground coal seams. *Int J Rock Mech Min Sci* 2013;58:34–45.
- [45] Weng X. Modeling of complex hydraulic fractures in naturally fractured formation. *J Unconventional Oil Gas Resour* 2015;9:114–35.
- [46] Weniger P, Kalkreuth W, Busch A, Krooss BM. High-pressure methane and carbon dioxide sorption on coal and shale samples from the Paraná Basin, Brazil. *Int J Coal Geol* 2010;84(3–4):190–205.
- [47] Yin H, Zhou J, Jiang Y, Xian X, Liu Q. Physical and structural changes in shale associated with supercritical CO₂ exposure. *Fuel* 2016;184:289–303.
- [48] Yin H, Zhou J, Xian X, Jiang Y, Lu Z, Tan J, Liu G. Experimental study of the effects of sub- and super-critical CO₂ saturation on the mechanical characteristics of organic-rich shales. *Energy* 2017;132:84–95.
- [49] Zhang M, de Jong SM, Spiers CJ, Busch A, Wentinck HM. Swelling stress development in confined smectite clays through exposure to CO₂. *Int J Greenhouse Gas Control* 2018;74:49–61.
- [50] Zhi S, Elsworth D, Liu L. W-shaped permeability evolution of coal with supercritical CO₂ phase transition. *Int J Coal Geol* 2019;211:1–14. <https://doi.org/10.1016/j.coal.2019.103221>.
- [51] Zhou J, Liu G, Jiang Y, Xian X, Liu Q, Zhang D, Tan J. Supercritical carbon dioxide fracturing in shale and the coupled effects on the permeability of fractured shale: an experimental study. *J Nat Gas Sci Eng* 2016;36:369–77.
- [52] Zhou J, Tian S, Zhou L, Xian X, Yang K, Jiang Y, Zhang C, Guo Y. Experimental investigation on the influence of sub- and super-critical CO₂ saturation time on the permeability of fractured shale. *Energy* 2020;191:116574. <https://doi.org/10.1016/j.energy.2019.116574>.
- [53] Tan J, Weniger P, Krooss B, Merkel A, et al. Shale gas potential of the major marine shale formations in the Upper Yangtze Platform, South China, Part II: Methane sorption capacity. *Fuel* 2014;129:204–18. <https://doi.org/10.1016/j.fuel.2014.03.064>.